FEATURE ARTICLE

Nanosphere Lithography: A Versatile Nanofabrication Tool for Studies of Size-Dependent Nanoparticle Optics

Christy L. Haynes and Richard P. Van Duyne*

Department of Chemistry, Northwestern University, Evanston, Illinois 60208-3113

Received: February 19, 2001

Nanosphere lithography (NSL) is an inexpensive, simple to implement, inherently parallel, high throughput, materials general nanofabrication technique capable of producing an unexpectedly large variety of nanoparticle structures and well-ordered 2D nanoparticle arrays. This article describes our recent efforts to broaden the scope of NSL to include strategies for the fabrication of several new nanoparticle structural motifs and their characterization by atomic force microscopy. NSL has also been demonstrated to be well-suited to the synthesis of size-tunable noble metal nanoparticles in the 20−1000 nm range. This characteristic of NSL has been especially valuable for investigating the fascinating richness of behavior manifested in size-dependent nanoparticle optics. The use of localized surface plasmon resonance (LSPR) spectroscopy to probe the size-tunable optical properties of Ag nanoparticles and their sensitivity to the local, external dielectric environment (viz., the nanoenvironment) is discussed in detail. More specifically, the effects of nanoparticle size, shape, interparticle spacing, nanoparticle-substrate interaction, solvent, dielectric overlayers, and molecular adsorbates on the LSPR spectrum of Ag nanoparticles are presented. This systematic study of the fundamentals of nanoparticle optics promises to find application in the field of chemical and biological nanosensors; herein, the initial data demonstrate that LSPR spectroscopy of Ag nanoparticles can be used to sense specifically bound analytes with zeptomole per nanoparticle detection limits and no detectable nonspecific binding.

1. Introduction

Currently, there is enormously widespread interest in nanomaterials and their size-dependent properties. This is clearly evident by the burgeoning number of publications and conferences on this subject. In addition to inherent intellectual curiosity, interest in this topic is driven by the needs of the microelectronics, data storage, and communications industries for ever smaller device feature sizes to meet the ever greater demand for improved performance and decreased cost.[1]

All physical and chemical properties are size-dependent at some length scale because the properties of individual atoms are profoundly different than that of bulk materials. There are three size regimes to consider in order to fully understand the physical and chemical properties of any material: bulk, nanoparticles/nanostructures,[2−8] and atomic clusters.[2,9−12] The boundaries between these three size regimes vary for each material and property being studied. The size-dependent properties that are often of interest include optical,[13−16] magnetic,[17,18] catalytic,[19−22] thermodynamic,[23,24] electrochemical,[25] and electrical transport.[5,26,27]

One particularly active area of interest is the size-dependent optical properties of noble metal nanoparticles. Previous work has demonstrated new optical filters,[28,29] substrates for surface-enhanced spectroscopies,[30−42] biosensors,[43−45] bioprobes,[46,47] chemical sensors,[48,49] and optical devices[50−57] based on nanoparticle optical properties. The signature optical property of a metallic nanoparticle is the localized surface plasmon resonance (LSPR). This resonance occurs when the correct wavelength of light strikes a metallic nanoparticle, causing the plasma of conduction electrons to oscillate collectively. The term LSPR is used because this collective oscillation is localized within the near surface region of the nanoparticle. The two consequences of exciting the LSPR are (1) selective photon absorption and (2) generation of locally enhanced or amplified electromagnetic (EM) fields at the nanoparticle surface. The LSPR for noble metal nanoparticles in the 20 to a few hundred nanometer size regime occurs in the visible and IR regions of the spectrum and can be measured by UV−visible−IR extinction spectroscopy.

The ideal nanofabrication technique for systematic study of size-dependent properties would be materials and substrate general; inexpensive; flexible in nanoparticle size, shape, and spacing parameters; and massively parallel. Several standard lithographic methods are routinely used to create nanostructures with controlled size, shape, and interparticle spacing. By far, the most widely used is photolithography;[58,59] however, it has not been widely applied to nanostructure fabrication as a consequence of its diffraction-limited resolution of ca. $\lambda/2$. The use of ultraviolet lasers,[60] holographic interferometry,[40−42,61] and high numerical aperture optics has significantly extended both its longevity and applicability to the sub-300 nm regime. Electron beam lithography[59] is characterized by low sample

* To whom correspondence should be addressed. E-mail: vanduyne@chem.nwu.edu

10.1021/jp010657m CCC: $20.00
Published on Web 05/09/2001

throughput, high sample cost, modest feature shape control, and excellent feature size control. X-ray lithography[62] is characterized by initially high capital costs but high sample throughput. The recent development of scanning tunneling microscopy[63] and atomic force microscopy[64,65] lithographic techniques show great promise. The challenge in scanning probe lithography is to overcome its inherent disadvantage of being a serial process. Consequently, several alternative, parallel nanolithographic techniques are being explored including (1) diffusion-controlled aggregation at surfaces,[66−68] (2) laser-focused atom deposition,[69] (3) chemical synthesis of metal-cluster compounds and semiconductor nanocrystals,[2] and (4) "natural lithography".[70,71]

The inception of "natural lithography" dates from the seminal work of Fischer and Zingsheim with the introduction of "naturally"-assembled polystyrene latex nanospheres as a mask for contact imaging with visible light in 1981.[71] In 1982, Deckman and co-workers greatly extended the scope of Fischer's approach by demonstrating that a self-assembled nanosphere monolayer could be used as both a material deposition and etch mask. Deckman coined the term "natural lithography" to describe this process. Deckman and co-workers continued to explore various fabrication parameters and possible applications of natural lithography but always employed a single layer (SL) of nanospheres as the mask.[70,72−76] The third stage in the evolution of natural lithography, renamed nanosphere lithography (NSL) to be more operationally descriptive, is represented by the work of Van Duyne et al., who extended the SL methodology with (1) the development of a double layer (DL) nanosphere mask, (2) atomic force microscopy (AFM) studies of SL and DL periodic particle arrays (PPAs) of Ag on mica, and (3) fabrication of defect-free SL and DL PPAs of Ag on mica with areas of 10−100 μm^2 that were large enough to permit microprobe studies of nanoparticle optical properties.[77] NSL is now recognized as an inexpensive (less than $1 per sample), inherently parallel, high-throughput, and materials general nanofabrication technique and is being used in laboratories around the world to study the size-dependent optical, magnetic, electrochemical, thermodynamic, and catalytic properties of materials.

The remainder of this paper is organized as follows. In section 2, the fabrication of eight different nanoparticle structural motifs and their characterization by atomic force microscopy is explored. Although many materials could have been used to illustrate the structural properties of NSL derived nanoparticles, Ag is presented throughout section 2 as the model system. The reason for choosing Ag as the model material, obvious in section 3, lies in the exquisite sensitivity of the LSPR to nanoparticle structure and both local and external dielectric environment (viz., the nanoenvironment). Specifically, the effects of nanoparticle size, shape, interparticle spacing, nanoparticle−substrate interaction, solvent, dielectric overlayers, and molecular adsorbates on the LSPR spectrum of Ag nanoparticles are presented. An important application of these fundamental studies, the development of chemical and biological nanosensors, will also be demonstrated. In section 4, our results and conclusions will be summarized.

2. Overview of Nanoparticle Structural Motifs Accessible by Nanosphere Lithography

NSL is a powerful fabrication technique to inexpensively produce nanoparticle arrays with controlled shape, size, and interparticle spacing.[77] The need for monodisperse, reproducible, and materials general nanoparticles has driven the development and refinement of the most basic NSL architecture as well as many new nanostructure derivatives. Every NSL structure begins with the self-assembly of size-monodisperse nanospheres of diameter D to form a two-dimensional colloidal crystal deposition mask. Methods for deposition of a nanosphere solution onto the desired substrate include spin coating,[77] drop coating,[78] and thermoelectrically cooled angle coating.[79] All of these deposition methods require that the nanospheres be able to freely diffuse across the substrate, seeking their lowest energy configuration. This is often achieved by chemically modifying the nanosphere surface with a negatively charged functional group such as carboxylate or sulfate that is electrostatically repelled by the negatively charged surface of a substrate such as mica or glass. As the solvent (water) evaporates, capillary forces draw the nanospheres together, and the nanospheres crystallize in a hexagonally close-packed pattern on the substrate. As in all naturally occurring crystals, nanosphere masks include a variety of defects that arise as a result of nanosphere polydispersity, site randomness, point defects (vacancies), line defects (slip dislocations), and polycrystalline domains. Typical defect-free domain sizes are in the 10−100 μm^2 range. Following self-assembly of the nanosphere mask, a metal or other material is then deposited by thermal evaporation, electron beam deposition (EBD), or pulsed laser deposition (PLD) from a source normal to the substrate through the nanosphere mask to a controlled mass thickness d_m. After metal deposition, the nanosphere mask is removed by sonicating the entire sample in a solvent, leaving behind the material deposited through the nanosphere mask to the substrate.

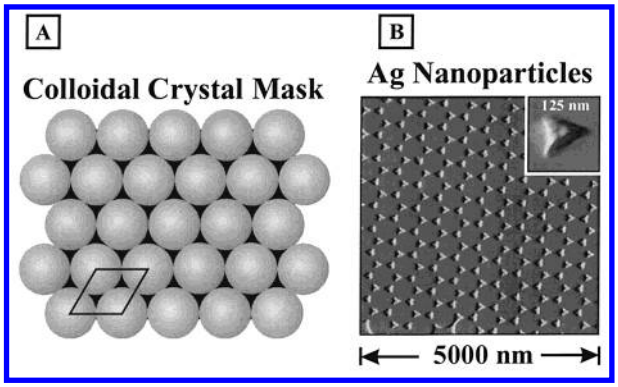

Figure 1. Schematic illustration (A) and representative AFM image (B) of SL PPA. The ambient contact mode AFM image was captured from a SL PPA fabricated with D = 542 nm nanospheres and d_m = 48 nm thermally evaporated Ag metal after 3 min sonication in methylene chloride.

Following a review of the structural characteristics of SL and DL nanoparticle arrays, the remainder of this section describes how nanoparticle size, shape, and arrangement can be significantly altered to form new structural motifs with only minor modifications to the NSL deposition technique.

2.1. Single Layer Periodic Particle Arrays. In the simplest NSL scenario, only a monolayer of hexagonally close-packed nanospheres is self-assembled onto the substrate. When one deposits metal through the monolayer mask, the three-fold interstices allow deposited metal to reach the substrate, creating an array of triangularly shaped nanoparticles with P_{6mm} symmetry (Figure 1). This array is referred to as a SL PPA. Simple geometric calculations define the relationship between the perpendicular bisector of the triangular nanoparticles, a, and the interparticle spacing, d_{ip}, to the nanosphere diameter.

$$a = \frac{3}{2}\left(\sqrt{3} - 1 - \frac{1}{\sqrt{3}}\right)D \qquad (1)$$

$$d_{ip} = \frac{1}{\sqrt{3}}D \quad (2)$$

In a SL PPA, nanoparticles cover 7.2% of the substrate area. The SL PPA is the most commonly used NSL-based nanostructure. Extensive studies of SL PPA optical properties are discussed in the section 3 of this paper.

2.2. Double Layer Periodic Particle Arrays. If one increases the concentration of nanospheres in the solution to be self-assembled onto the substrate, a significant portion of the colloidal crystal will consist of DLs of hexagonally close-packed nanospheres. When a second layer of nanospheres assembles onto the first, every other three-fold hole is blocked, and a smaller density of six-fold interstices results. After depositing metal through the DL nanosphere mask, the mask is removed, and a regular pattern of hexagonal nanoparticles remains on the substrate (Figure 2). This array is referred to as a DL PPA. As in the SL PPA, the size of the DL PPA nanoparticles can be tuned by the deposited nanosphere size and the d_m. Simple geometric calculations define the relationship between the diameter of the hexagonal nanoparticles, a, and the interparticle spacing, d_{ip}, and the nanosphere diameter.

$$a = \left(\sqrt{3} - 1 - \frac{1}{\sqrt{3}}\right)D \quad (3)$$

$$d_{ip} = D \quad (4)$$

In the DL PPA scenario, the nanoparticles cover 2.2% of the substrate area. There are two possible outcomes when a third layer of nanospheres assembles onto a DL: (1) if the nanospheres pack in an ABAB sequence, the regular pattern of hexagonal holes remains or (2) if the nanospheres pack in an ABCABC sequence, all of the mask holes are blocked. Therefore, a nanosphere mask containing three or more layers in the ABCABC stacking sequence does not allow any deposited material to reach the substrate.

An extremely promising application of the DL PPA architecture lies in the area of magnetic nanomaterials for data storage. The data storage industry desires decreasing bit sizes and increasing bit densities, making magnetic nanoparticles a good prospect.[18] Like all physical properties, magnetic properties are size-dependent. As magnetic materials reach the size regime of 100−500 nm, the physical size of the magnet dictates that the lowest energy structure is one in which all magnetic moments point in the same direction, creating a single domain magnet. Magnetic force microscopy (MFM) investigations [80,81] of high areal density DL PPAs show that single domain magnetic nanoparticles can be fabricated with the NSL technique. Because nanoscale single domain magnets will act as the most efficient "ones" and "zeros" in binary data storage, the single or multiple domain character of magnetic DL PPA nanoparticles has large implications in data storage capability.

2.3. Nanorings. In the process of creating SL and DL PPAs for magnetic and catalytic studies using transition metals (nickel, cobalt, platinum, and palladium), a third NSL structural motif, the nanoring, was discovered. The high melting points of the transition metals require that they be deposited by EBD or PLD rather than thermal evaporation to avoid melting the polystyrene nanospheres used to form the NSL mask. An array of nanorings within a SL PPA formed by EBD of nickel is shown in Figure 3. The detailed mechanism of nanoring formation is not currently known. We are, however, reasonably certain of two facts: (1) the nanorings are formed from nickel (or nickel oxide) because they display magnetic contrast in MFM images and (2) the nanorings are never formed when thermal evaporation is used to deposit material. Our current hypothesis concerning the nanoring formation mechanism centers on the bimodal kinetic energy distribution of gas-phase atoms produced by EBD and PLD. Low kinetic energy (∼0.1 eV) atoms that travel along a direct line of sight from the EBD or PLD target to the substrate and stick where they strike the substrate form the triangular nanoparticles. In contrast, high kinetic energy (∼1−10 eV) atoms that travel along off-normal trajectories strike the substrate within the "footprint" of the triangular interstices of the nanosphere mask, and then continue to travel, because of excess kinetic energy, adhering to the substrate underneath the nanosphere to form the nanorings. We have not yet explored any nanoring properties; however, we suggest that they may find future applications as optical traps, components of nanomachines, and reactive ion etch masks to form thin-walled nanocylinders.

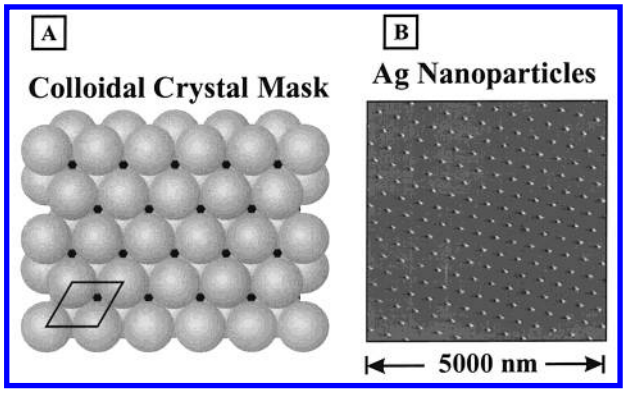

Figure 2. Schematic illustration (A) and representative AFM image (B) of DL PPA. The ambient contact mode AFM image was captured from a SL PPA fabricated with $D = 400$ nm nanospheres and $d_m = 30$ nm thermally evaporated Ag metal after three minutes sonication in methylene chloride.

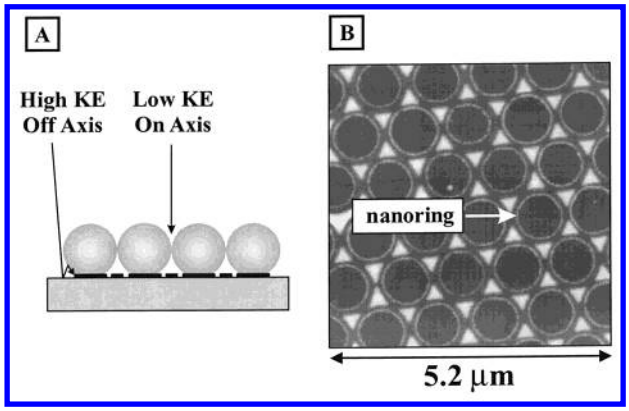

Figure 3. Schematic illustration (A) and representative AFM image (B) of nanoring and SL PPA fabrication. The ambient contact mode AFM image was captured from a sample fabricated with $D = 979$ nm nanospheres and $d_m = 50$ nm e-beam deposited Ni metal after three minutes sonication in methylene chloride.

2.4. Single Layer Periodic Particle Arrays as Templates for Covalently Attached Nanoparticle Assemblies. The three NSL-derived nanoparticle structural motifs described above are two-dimensional in character. Recently, an exploratory study aimed at extending NSL into the third dimension has been carried out.[82] The fabrication strategy employed begins with a Ag or Au SL PPA (Figure 4A) as a template upon which to build more complex nanoparticle assemblies. The proposal is then to covalently attach chemically synthesized Ag or Au colloids to the SL PPA template with bifunctional self-assembled monolayer (SAM) linkers. Structural characterization of this

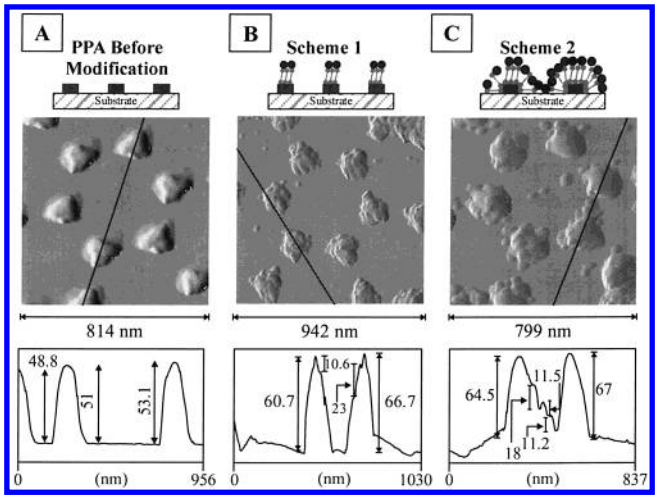

Figure 4. Schematic illustrations and tapping mode AFM images of colloid-modified SL PPA samples (D = 400 nm and d_m = 50 nm). (A) Unmodified Ag SL PPA, (B) top face only modification of Ag SL PPA with 13 nm diameter Au colloids, and (C) four face modification of Ag SL PPA with 13 nm diameter Au colloids.

three-dimensional nanoparticle-linker-SL PPA assembly is afforded by quantitative analysis of AFM line scan data.

Two variants of this nanofabrication strategy are illustrated schematically in Schemes 1 and 2 of Figure 4. In Scheme 1, the PPA nanoparticles are dosed with the SAM linker prior to nanosphere mask removal, whereas in Scheme 2 the nanosphere mask is removed before exposure of the PPA nanoparticles to the linker. Following linker dosing and nanosphere removal, both schemes involve incubating the sample in a solution containing 10−15 nm diameter gold or silver colloids. Panels B and C of Figure 4 show AFM images and line scan data taken from samples fabricated according Schemes 1 and 2, respectively. The AFM image in Figure 4B clearly shows that the colloids are predominately attached to the top surface of the PPA nanoparticles. This is confirmed by the AFM line scan (bottom panel, Figure 4B) showing the ∼10 nm height increments corresponding to the attached colloids. This surprising result implies that the bifunctional SAM linker chemically modified only the top surface of the SL PPA nanoparticles. It is hypothesized that this anisotropic labeling of the top surface of SL PPA nanoparticles is a consequence of PPA nanoparticle sidewall shielding by the nanosphere mask and/or highly directional diffusion of the SAM linker. Elaboration of this anisotropic labeling methodology should provide the ability to chemically modify the top and the sides of PPA nanoparticles with different adsorbates. Studies of these bifunctional nanoparticles using surface-enhanced Raman spectroscopy (SERS) should yield exciting new insights into the dependence of the surface enhancement factor on adsorbate position. Perhaps this approach, or a variant thereof, will permit the visualization of the surface site(s) responsible for the enormous enhancement factors (viz., $10^{14} - 10^{15}$) associated with single molecule SERS.[83−85]

2.5. Angle-Resolved Nanosphere Lithography: Nanooverlaps, Nanogaps, and Nanoparticle Chains. In the aforementioned nanoparticle architectures, all materials were deposited from a collimated source along a line perpendicular to the plane of the nanosphere mask. A new class of NSL structures has been fabricated by varying the angle, θ_{dep}, between the nanosphere mask and the beam of material being deposited. This technique is hereafter referred to as angle-resolved NSL (AR NSL). Control of the deposition angle has been used previously to produce other nanofabricated surfaces, such as field effect

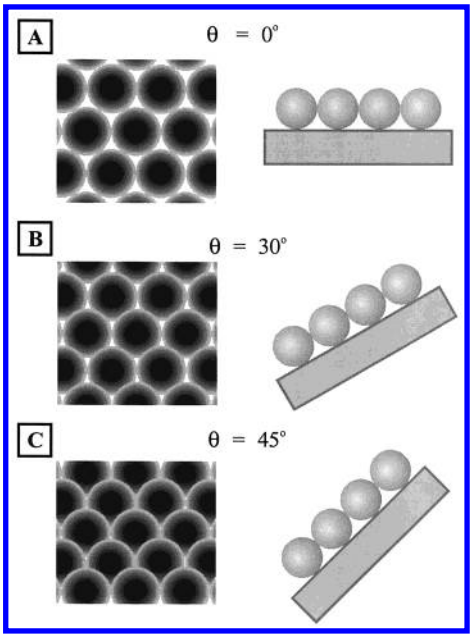

Figure 5. Schematic of the angle resolved deposition process. (A) Samples viewed at 0°. The interstices in the nanosphere mask are equally spaced and of equal size. (B) Sample viewed at 30°. The interstices in the nanosphere mask follow a pattern including two different interparticle spacing values, and the interstitial area is smaller. (C) Sample viewed at 45°. The interstices are now closed to line of sight deposition.

transistors,[86,87] single electron transistors,[88] ultrasmall tunnel junctions,[89,90] and optical coatings.[91]

The size and shape of the three-fold interstices of the nanosphere mask change relative to the deposition source as a function of θ_{dep}, and accordingly, the deposited nanoparticles' shape and size is controlled directly by θ_{dep} (Figure 5). As a convention, θ_{dep} = 0° represents a substrate mounted normal to the evaporation beam, and all variations of θ_{dep} are made by mounting the substrates on machined aluminum blocks. Figure 5 schematically depicts the effect of angle-resolved deposition on the interstices of a NSL mask from the top view. It is clear from this illustration that an increase in θ_{dep} causes the projections of the interstices onto the substrate to decrease and shift. At high values of θ_{dep}, the projections of the interstices close, completely blocking the substrate to line of sight deposition. There is an analogous decrease in size and shift of interstitial projections when the DL nanosphere mask is rotated through nonzero θ_{dep} values.

One very important consequence of AR NSL, beyond the increased flexibility in nanostructure architecture, lies in the decrease in nanoparticle size. The demand for nanostructures in the 1−20 nm size regime is being driven by the ever decreasing feature size requirements of devices in the microelectronics industry and the recognition that molecular connections may play an important role in the future of this industry. An additional driver is the recognition that molecular electronic devices and interconnects are likely to play a role in the future of this industry. Before AR NSL, the only way to fabricate nanoparticles in the 1−20 nm size regime with NSL required self-assembly of nanospheres with diameters on the order of 5−100 nm. Self-assembly of such small nanospheres into well-ordered 2D arrays is difficult because of problems with greater polydispersity and, for nanospheres chemically derivitized with charged functional groups, greater charge density. However, with AR NSL, increasing θ_{dep} from 0° to 20° will halve the in-plane dimension of both SL and DL PPA nanoparticles, eliminating the difficulty in small nanoparticle preparation.

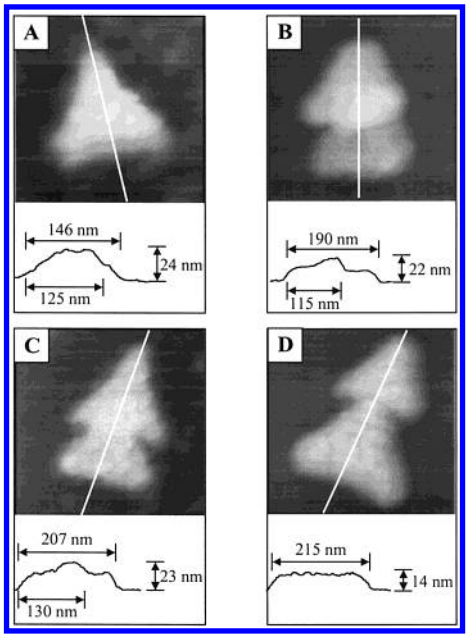

Figure 6. Contact mode AFM images of Ag SL PPA nanooverlap structures fabricated on mica substrates. All reported line scan values have not been deconvoluted for tip broadening effects. (A) 300 nm × 300 nm image, $D = 542$ nm, $d_m = 20$ nm, $\theta_{dep} = 0°$ and 6°. (B) 250 nm × 250 nm image, $D = 542$ nm, $d_m = 20$ nm, $\theta_{dep} = 0°$ and 10°. (C) 300 nm × 300 nm image, $D = 542$ nm, $d_m = 20$ nm, $\theta_{dep} = 0°$ and 15°. (D) 250 nm × 250 nm image, $D = 542$ nm, $d_m = 20$ nm, $\theta_{dep} = 0°$ and 20°.

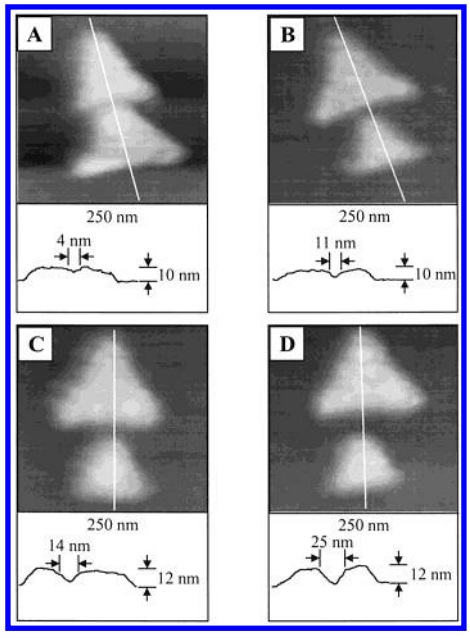

Figure 7. Contact mode AFM images of Ag SL PPA nanogap structures fabricated on mica substrates. All reported line scan values have not been deconvoluted for tip broadening effects. (A) 250 nm × 250 nm image, $D = 542$ nm, $d_m = 20$ nm, $\theta_{dep} = 0°$ and 22°. (B) 250 nm × 250 nm image, $D = 542$ nm, $d_m = 20$ nm, $\theta_{dep} = 0°$ and 23°. (C) 250 nm × 250 nm image, $D = 542$ nm, $d_m = 20$ nm, $\theta_{dep} = 0°$ and 24°. (D) 250 nm × 250 nm image, $D = 542$ nm, $d_m = 20$ nm, $\theta_{dep} = 0°$ and 26°.

Although AR NSL can be used to fabricate nanoparticles of varied shape and size by single deposition through SL and DL masks, additional nanoparticle structural motifs are possible with multiple depositions of a single material, or multiple materials, through a single nanosphere mask. By varying θ_{dep} between two depositions, both nanooverlap and nanogap structures can be produced.

2.5.1. Nanooverlap Structures. Nanooverlap structures are fabricated by first depositing material through a nanosphere mask mounted at $\theta_{dep} = 0°$ and then depositing a second layer of material at or below an overlap threshold value of θ_{dep}. In the examples shown here, all samples have Ag metal thermally evaporated through a nanosphere mask with $D = 542 \pm 7$ nm onto mica substrates. In this case, the amount of nanoparticle overlap decreases as θ_{dep} is increased from 0° to 20°, at which point neither overlap nor gap is visible by AFM investigation (Figure 6).

The most likely application of nanooverlap structures will focus on the optical properties of these very large aspect ratio (in-plane width/out-of-plane height) nanoparticles. Section 3.6 provides full detail of the increased sensitivity of optical response as the nanoparticle aspect ratio is increased. Nanooverlap structures allow predictable aspect ratio increases up to double the original value.

2.5.2. Nanogap Structures. Nanogap structures are fabricated by first depositing material through a nanosphere mask mounted at $\theta_{dep} = 0°$ and then depositing a second layer of material at or above a nanogap threshold value of θ_{dep}. With the same experimental parameters defined above, the gap between nanoparticles increases as θ_{dep} is increased from 22° to higher values (Figure 7) up to the θ_{dep} value at which the interstitial projections are closed to line-of-sight deposition.

Work is in progress to use the nanogap architecture to measure the electrical conductivity of a single molecule or nanoparticle. Because NSL is a materials-general technique, the deposition materials in multiple deposition experiments need not be the same. If one side of the nanogap is insulated from a conductive substrate while the other side of the nanogap is in contact with a conductive substrate, the conductance of the junction should be measurable with a scanning tunneling microscopy probe. The proposed nanoparticle architecture has been fabricated, and results will be presented elsewhere. Experiments such as single molecule electrical conductivity are made possible by the advantages of AR NSL including (1) high resolution of nanoparticle manipulation, (2) simple geometric prediction of nanogap size, (3) parallel creation of millions of nanogaps on one substrate, and (4) choice of nanoparticle materials to favor the attachment chemistry of each molecule to be investigated.

It is possible to quantitate the resolution of nanoparticle manipulation by plotting the θ_{dep} versus the measured overlap or gap in nanometers and fitting a curve to these data points (Figure 8). With the aforementioned experimental parameters, the derivative of the curve at the point where the two nanoparticles are neither overlapped nor separated (in this case, $\theta_{dep} = 21.42°$) is equal to 7.5 nm/degree. The implication of this slope is that angle control to the level of $\theta_{dep} = \pm 0.1°$ yields nanogap fabrication with 0.75 nm resolution.

It must be noted that the AFM images of all of the AR NSL samples depicted here have the sample tilt axis aligned with the perpendicular bisector of the nanoparticle for the sake of simplicity. Other nanoparticles, within another domain on the same sample, have the tilt axis aligned with the base of the triangular nanoparticle or at intermediate alignments.

2.5.3. Nanoparticle Chains. Clearly, if two depositions at different values of θ_{dep} extend the range of nanoparticle architectures accessible by AR NSL, three or more depositions will extend it further. An endless number of nanostructures are possible when one combines the ability to vary θ_{dep} and to perform multiple material depositions. A simple but potentially

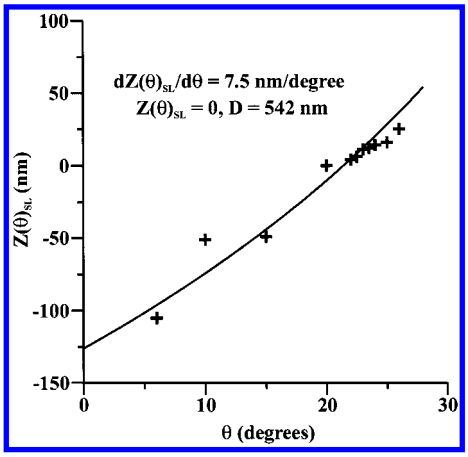

Figure 8. Plot of the predicted nanooverlap/nanogap, $Z(\theta)_{SL}$, as a function of angle assuming a nanosphere size D equal to 542 nm. At the point where $Z(\theta)_{SL}$ is equal to 0 nm ($\theta = 21.42°$), the derivative of the curve is equal to 7.5 nm/degree.

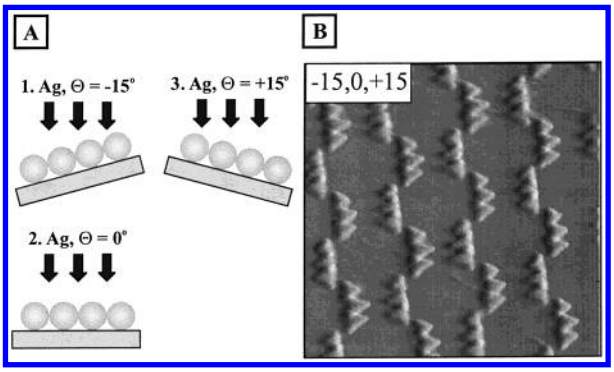

Figure 9. Schematic illustration (A) and contact mode AFM image (B) of three deposition nanochain structure on mica. 1.6 μm × 1.6 μm area, $D = 542$ nm, $d_m = 10$ nm, $\theta_{dep} = +15°$, 0°, and $-15°$.

useful example is presented here. The nanochain motif is fabricated with three consecutive depositions. The first deposition is done at $\theta_{dep} = 0°$, whereas the second and third depositions are done at $\theta_{dep} = 15°$ (tilted forward) and $\theta_{dep} = -15°$ (tilted backward). An AFM image of the nanochain structure is shown in Figure 9 and depicts a domain where the sample tilt axis is aligned with the triangular base of the nanoparticles. Possible applications of the nanochain architecture include sub-100 nm near-field optical waveguides, chemical and biological sensors based on the LSPR of these high aspect ratio nanoparticles, and the fabrication of nanowires.

The work described above demonstrates that NSL, broadly defined to include AR NSL and other variants, is manifestly capable of creating far more than arrays of nanotriangles and nanodots as was once supposed. In addition we have alluded to a variety of near-future and far-future applications ranging from chemical and biological sensors to nanooptical devices and nanoelectronic components. The combination of the diversity of nanostructures accessible by NSL coupled to its ease of implementation, low cost, etc. lead us to conclude that NSL has a bright future. In the next section, the ability of NSL to synthesize monodisperse, size-tunable nanoparticles will be exploited to investigate the size-dependent nanoparticle optics of the SL PPA structure. LSPR spectroscopy will be used to probe the size-tunable optical properties of Ag nanoparticles and their sensitivity to the local, external dielectric environment (viz., the nanoenvironment).

3. Localized Surface Plasmon Resonance Spectrum of Ag Nanoparticles and Its Sensitivity to Structure and Nanoenvironment

The initial motivation for fabricating surfaces with well-defined, periodic nanostructures was to gain a better understanding of the enhancement mechanism(s) of surface-enhanced Raman scattering (SERS).[92−95] The EM enhancement mechanism proposes that the collective oscillation of conduction electrons absorbs and scatters photons meeting the resonance condition. As a consequence, strongly amplified local EM fields are generated at the nanoparticle surface. The absorbed and scattered light from nanoparticle surfaces can be monitored by optical extinction spectroscopy in either transmission or reflection geometry. In the case of the Ag nanoparticles considered in this article, the relevant wavelength range of these extinction spectroscopy experiments can extend from the near-ultraviolet (~300 nm) for Ag nanospheres ~10 nm in diameter to the mid-infrared (~10 000 nm) for Ag nanotriangles with large aspect ratios. Extinction spectroscopy conveniently correlates nanoparticle structure with the readily measured LSPR observables.

The simplest theoretical approach available for modeling the extinction properties of nanoparticles is the Mie theory estimation of the extinction of a metallic sphere in the dipole limit. In the following equation[96]

$$E = \frac{24\pi^2 N_A a^3 \epsilon_m^{3/2}}{\lambda \ln(10)}\left[\frac{\epsilon_i}{(\epsilon_r + 2\epsilon_m)^2 + \epsilon_i^2}\right] \quad (5)$$

E is the extinction which is, in turn, equal to the sum of absorption and Rayleigh scattering, N_A is the areal density of nanoparticles, a is the radius of the metallic nanosphere, ϵ_m is the dielectric constant of the medium surrounding the metallic nanosphere (assumed to be wavelength independent), λ is the wavelength of the absorbing radiation, ϵ_i is the imaginary portion of the metallic nanosphere's dielectric function, and ϵ_r is the real portion of the metallic nanosphere's dielectric function. Even in this most primitive model, it is abundantly clear that the experimental extinction spectrum of an isolated metallic nanosphere imbedded in an external dielectric medium will depend on nanoparticle radius a, nanoparticle material (ϵ_i and ϵ_r), and the nanoenvironment's dielectric constant (ϵ_m). Furthermore, when the nanoparticles are not spherical, as is always the case in real samples, the extinction spectrum will depend on the nanoparticle's in-plane diameter, out-of-plane height, and shape. The dependence of the extinction spectrum on these nanoparticle structural characteristics has also been recognized in the form of simplified model calculations such as those for ellipsoidal nanoparticle geometries.[97] In addition, the samples considered here contain an ensemble of nanoparticles that are supported on a substrate. Thus, the extinction spectrum will also depend on interparticle spacing and substrate dielectric constant. Finally, the nanoparticles under study may also possess an intentionally deposited thin dielectric or molecular adsorbate overlayer. The dielectric overlayer may function to provide chemical protection for the nanoparticle surface or be a molecularly selective permeation layer to control molecular access to the surface. Molecular adsorbates may be physisorbed or chemisorbed and, in the case of surface-enhanced Raman spectroscopic experiments, are the target of study. Consequently, the extinction spectrum will depend on a variety of parameters such as dielectric overlayer thickness and dielectric constant and molecular adsorbate dielectric constant, thickness, and coverage which will be referred to, collectively, as the nanoenvironment.

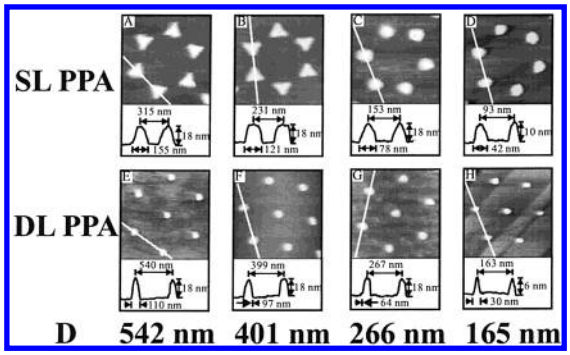

Figure 10. AFM images and line scans of representative Ag nanoparticle arrays on mica substrates. The line scan values reported here have not been deconvoluted for tip broadening effects. (A) 870 nm × 870 nm image, $D = 542$ nm, $d_m = 18$ nm; (B) 610 nm × 610 nm image, $D = 401$ nm, $d_m = 18$ nm; (C) 420 nm × 420 nm image, $D = 264$ nm, $d_m = 18$ nm; (D) 260 nm × 260 nm image, $D = 165$ nm, $d_m = 14$ nm; (E) 1200 nm × 1200 nm image, $D = 542$ nm, $d_m = 18$ nm; (F) 1000 nm × 1000 nm image, $D = 401$ nm, $d_m = 18$ nm; (G) 670 nm × 670 nm image, $D = 264$ nm, $d_m = 18$ nm; (H) 410 nm × 410 nm image, $D = 165$ nm, $d_m = 0.5$ nm.

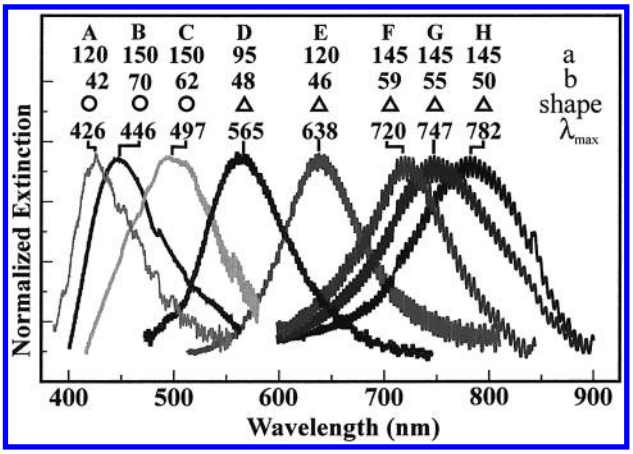

Figure 11. UV−visible extinction spectra of Ag SL PPA on mica substrates. Reported spectra are raw, unfiltered data. The oscillatory signal superimposed on the LSPR spectrum seen in the data is due to interference of the probe beam between the front and back faces of the mica.

In the next section, the broad range of materials that have been used to fabricate nanoparticles by NSL is discussed. Following this, sections 3.2−3.8 focus on Ag nanoparticles and discuss in substantial detail the dependence of the LSPR spectrum, as revealed by extinction spectroscopy, on size, shape, interparticle spacing, substrate, and dielectric nanoenvironment. Such an exhaustive, systematic study was not previously feasible because of a lack of independent experimental control over this broad parameter space. NSL is the enabling tool that now makes it possible to independently investigate the dependence of the LSPR on nanostructure and nanoenvironment. It is now our position that surface-enhanced Raman spectroscopic data is difficult, if not impossible, to correctly interpret without understanding the concepts presented herein.

3.1. Effect of Nanoparticle Material on the LSPR. Any material that can be deposited from the gas phase can be used to form SL and DL PPAs, AR PPAs, nanogap, nanooverlap, or nanochain architectures. Within the last 10 years, there have been examples of NSL structures fabricated from the inorganic materials Ag, Al, Au, Co, Cr, Cu, Fe, In, KBr, MgF_2, NaCl, Ni, Pd, Pt, Rh, SiO_x, and Zn. The first nanoparticles fabricated from an organic material, cobalt phthalocyanine (CoPc), were also fabricated using the NSL technique.[77] Experiments are currently in progress to systematically study the nanoparticle optics of the many material systems capable of supporting a LSPR. However, in the following sections, attention is focused exclusively on the remarkable nanoparticle optics of silver.

3.2. Effect of Nanoparticle Size on the Ag LSPR. The relationship between nanoparticle size and the LSPR extinction maximum, λ_{max}, has been recognized, though not fully understood, for many years. As atomic force microscopy, scanning electron microscopy, and tunneling electron microscopy have become standard laboratory techniques, nanoparticle dimensions have been determined and electrodynamic theory is helping to explain the experimental light scattering and absorption trends. NSL is particularly useful in this regard because nanoparticle size is easily varied by changing the nanosphere mask diameter, D, and the deposited mass thickness, d_m. The dimensions of each nanoparticle in the SL PPA is defined by two parameters: (1) the length of the triangle's perpendicular bisector a and (2) the measured out-of-plane height b. As seen earlier, NSL is particularly useful because both large and small size extremes are accessible with the NSL technique (Figure 10). Very large nanoparticles (for example, with $a = 830$ nm and $b = 50$ nm) absorb and scatter light in the near-infrared and mid-infrared region of the spectrum.[98,99] The smallest DL PPA nanoparticles, with $a = 21$ nm and $b = 4$ nm, contain only 4×10^4 atoms and allow investigation of surface cluster properties.[78]

3.3. Effect of Nanoparticle Shape on the Ag LSPR. Nanoparticle shape also has a significant effect on the λ_{max} of the LSPR. When the standard triangular SL PPA nanoparticles are thermally annealed at 300 °C under vacuum, the nanoparticle shape is modified, increasing in out-of-plane height and becoming ellipsoidal. This structural transition results in a blue shift of ∼200 nm in the λ_{max} of the LSPR. It is often difficult to decouple size and shape effects on the LSPR wavelength, and so they are considered together as the nanoparticle aspect ratio (a/b). Large aspect ratio values represent oblate nanoparticles, and aspect ratios with a value of unity represent spheroidal nanoparticles.

Figure 11 shows a series of extinction spectra collected from Ag SL PPAs of varied shapes and aspect ratios on mica substrates. These extinction spectra were recorded in standard transmission geometry using either a Beckman DU-7, Ocean Optics SD2000, or an OLIS modified Cary 14 spectrophotometer. Regardless of the instrument used, all macroextinction measurements were recorded using unpolarized light, with a probe beam size of approximately 2−4 mm^2. All parameters, except those listed explicitly in Figure 11, were held constant throughout this series of measurements. To identify each parameter's effect on the LSPR, one must examine three separate cases. First, extinction peaks F, G, and H all have the same a value (signifying that the same diameter nanosphere mask was used for each sample), but the b value is varied as the shape is held constant. Note that the LSPR λ_{max} shifts to the red as the out-of-plane nanoparticle height is decreased, i.e., the aspect ratio is increased. Second, extinction peaks D, E, and H have varying a values, very similar b values, and a constant shape. In this case, the LSPR λ_{max} shifts to the red with increased nanosphere diameter (a larger a value). Again, as the aspect ratio increases, the LSPR shifts to longer wavelengths. Finally, extinction peaks C and F were measured from the same sample before and after thermal annealing. Note the slight increase in nanoparticle height (b) as the annealed nanoparticle dewets the mica substrate. The 223 nm blue shift upon annealing is in accordance with the decreasing nanoparticle aspect ratio as the nanoparticles transition from oblate to ellipsoidal geometries.

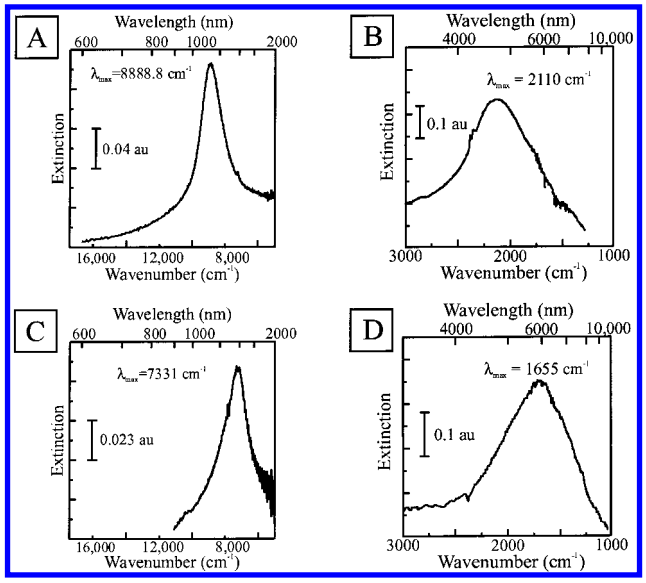

Figure 12. Near/mid infrared extinction spectra of Ag SL PPA on varied substrates. Reported spectra are raw, unfiltered data. (A) $D = 820 \pm 15$ nm, $d_m = 20$ nm, glass substrate; (B) $D = 2700 \pm 70$ nm, $d_m = 65$ nm, silicon substrate; (C) $D = 1100 \pm 15$ nm, $d_m = 25$ nm, glass substrate; (D) $D = 2542 \pm 80$ nm, $d_m = 50$ nm, germanium substrate.

The range of possible LSPR λ_{max} values extends beyond those shown in Figure 11. In fact, λ_{max} can be tuned continuously from ~400 to 6000 nm (Figure 12) by choosing the appropriate nanoparticle aspect ratio and geometry.[99] Recent experiments exploring the sensitivity of the LSPR λ_{max} to changes in a and b values support the assertion that it is not always possible to decouple the in-plane width and out-of-plane height from one another. Figure 11 demonstrates an in-plane width sensitivity of $\Delta\lambda_{max}/\Delta a = 4$ and an out-of-plane height sensitivity of $\Delta\lambda_{max}/\Delta b = 7$. To further investigate the out-of-plane height sensitivity, a larger data set was collected in the $\lambda_{max} = 500-600$ nm region using Ag SL PPA masks made from $D = 310 \pm 7$ nm nanospheres.[99] In this case, both the in-plane width and the shape were held constant as the nanoparticle height was varied. From this larger data set, the calculated out-of-plane height sensitivity was $\Delta\lambda_{max}/\Delta b = 2$. The variance in the two $\Delta\lambda_{max}/\Delta b$ values suggests that nanoparticles with smaller in-plane widths ($a = 90 \pm 6$ nm versus $a = 145 \pm 6$ nm) are less sensitive to changes in nanoparticle height. This conclusion supports the relationship between nanoparticle aspect ratio and LSPR shift susceptibility noted above.

3.4. Effect of Interparticle Spacing on the Ag LSPR. EM coupling between nanoparticles must also be considered in a well-designed experiment. If two nanoparticles are in close proximity, the conduction electron oscillation of each nanoparticle is affected by its coupling partner, causing the LSPR λ_{max} to shift. This coupling can be extensive and complicated. To determine the degree of EM coupling in SL PPAs, a theoretical simulation was done in which the λ_{max} of the LSPR was calculated as a function of the tip to tip distance (d_{tt}) between two triangular nanoparticles (Figure 13).[100] The plot shown in Figure 13 represents $d_m = 50$ nm Ag through a $D = 400 \pm 7$ nm nanosphere mask. The EM coupling is substantial when the two triangles are within 50 nm of one another. To apply this theoretical simulation to experimental data, the AFM measured SL PPA $d_{tt} = 114$ nm is explicitly marked by a dashed line in Figure 13. This value indicates a very small EM coupling between SL PPA nanoparticles, producing a red shift of only 5 nm. Therefore, the SL PPA nanostructure is considered to be largely uncoupled. Analogous analysis of the DL PPA nanostructure indicates an even smaller degree of EM coupling between nanoparticles.

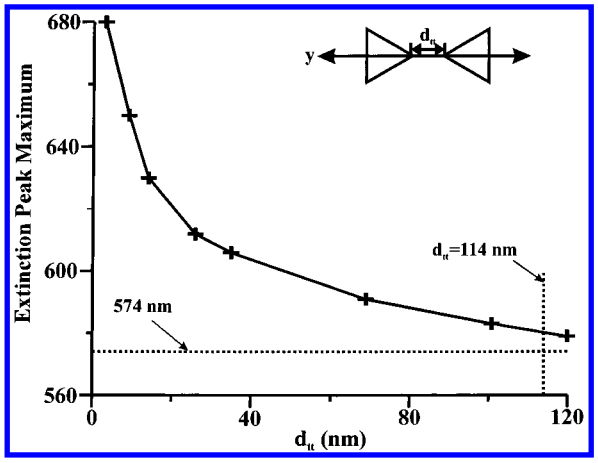

Figure 13. Effect of nanoparticle−nanoparticle interaction on the extinction spectrum of two truncated tetrahedra. The extinction peak maximum is plotted as a function of d_{tt}. Results are calculated using the discrete dipole approximation with 10 234 dipoles in each nanoparticle, dielectric constants from Palik, and polarization along the y axis. The solid lines are a guide for the eye.

EM coupling and, accordingly, a red shift in the LSPR λ_{max} can be explored using AR NSL experiments where the d_{tt} between two nanoparticles is greatly decreased. Recent experiments in our laboratory have shown that two deposition nanooverlap structures act as one high aspect ratio nanoparticle. It is anticipated that three deposition nanochain structures should further extend the LSPR red shift.

3.5. Effect of the External Dielectric Medium on the Ag LSPR. Next, the role of the external dielectric medium on the optical properties of these surface-confined nanoparticles is considered. Just as it is difficult to decouple the effects of size and shape from one another, the dielectric effects of the substrate and external dielectric medium (i.e., bulk solvent) are inextricably coupled because together they describe the entire dielectric environment surrounding the SL PPA. The nanoparticles are surrounded on one side by the substrate and on the other four sides by a chosen environment. A systematic study of the relationship between the LSPR λ_{max} and the external dielectric constant on the four non-substrate-bound faces of the nanoparticles was done by immersing a series of varied aspect ratio SL PPA samples (aspect ratios 3.32, 2.17, and 1.64) in a variety of solvents.[101] These solvents represent a progression of refractive indices: nitrogen (1.0), acetone (1.36), methylene chloride (1.42), cyclohexane (1.43), and pyridine (1.51). Each sample was equilibrated in a N_2 environment before solvent treatment. Extinction measurements were made before, during, and after each solvent cycle. With the exception of pyridine, the LSPR peak always shifted back to the N_2 value when the solvent was purged from the sample cell. The measured LSPR λ_{max} values progress toward longer wavelengths as the solvent refractive index increases (Figure 14). A plot of solvent refractive index versus the LSPR λ_{max} shift is linear for all three aspect ratio samples (Figure 15). The highest aspect ratio nanoparticles (most oblate) demonstrate the greatest sensitivity to a external dielectric environment. In fact, the LSPR λ_{max} of the 3.32 aspect ratio SL PPA shifts 200 nm per refractive index unit (RIU).

After completing the aspect ratio/solvent sensitivity experiment, a duplicate of the 2.17 aspect ratio SL PPA sample was

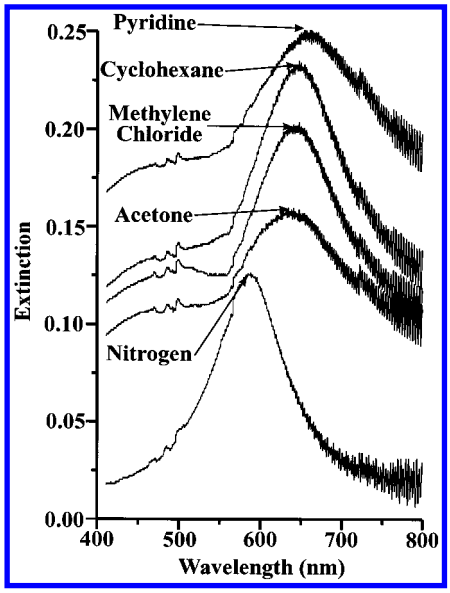

Figure 14. Extinction spectra of aspect ratio 2.17 Ag SL PPA measured in various solvents. Spectra have been arbitrarily spaced along the extinction axis for clarity.

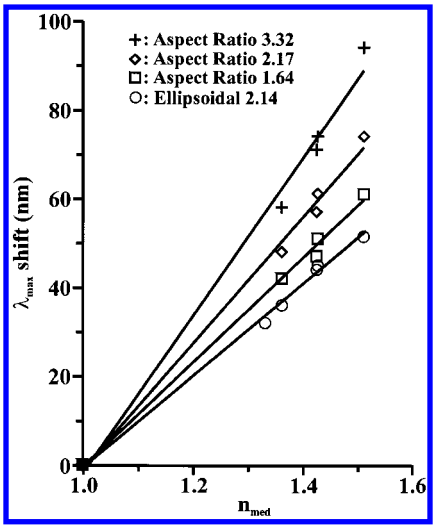

Figure 15. LSPR λ_{max}(solvent) − λ_{max}(dry N_2) versus the refractive index of the solvent for unannealed aspect ratios 3.32, 2.17, and 1.64 and annealed aspect ratio 2.14 Ag SL PPA samples.

thermally annealed. This annealed sample, with an aspect ratio of 2.14, was then subjected to the same series of solvent treatments and extinction measurements. The resultant solvent refractive index versus LSPR λ_{max} shift still shows a linear trend but a significantly decreased sensitivity of 100 nm shift per RIU (Figure 15).

3.6. Effect of Thin Film Dielectric Overlayers on the LSPR. The dielectric environment of the nanoparticles in the aforementioned experiments had two components: substrate on one face and solvent or N_2 on the other four faces. Clearly, the LSPR λ_{max} can be tuned by choosing the refractive index of an encapsulating solvent. Another means of controlling the nanoenvironment is to encapsulate the Ag nanoparticle in a thin film dielectric shell. Such a dielectric overlayer could function to provide chemical protection for the nanoparticle surface or be a molecularly selective permeation layer to control molecular access to the surface of the nanoparticle. A study of the effect of nanoparticle encapsulation made use of varying thicknesses of SiO_x overlayers. The SiO_x overlayer system presents a more complex dielectric environment including the substrate, the porous SiO_x, and the environment above the SiO_x layer. SiO_x overlayer thicknesses of 0, 15, 26, and 36 nm were vapor deposited onto otherwise identical SL PPA samples. The LSPR λ_{max} red shifted as the ratio of SiO_x to air increased (Figure 16a), again showing that an increased refractive index decreases the frequency of electron oscillation. By plotting the SiO_x thickness versus the LSPR λ_{max} peak shift, one concludes that the LSPR peak linearly shifts 4 nm to the red for every 1 nm of deposited SiO_x (Figure 16b). It was demonstrated in section 3.3 that the LSPR λ_{max} can be tuned from ~400 to 6000 nm by changing the size and shape of the nanoparticle. Now, it is obvious that dielectric tuning with substrate, solvent, and overlayers will also provide a similar range of LSPR λ_{max} values.

3.7. Effect of the Substrate Dielectric Constant on the LSPR. A systematic study was also done with Ag SL PPA nanoparticles holding all parameters constant with the exception of the substrate.[102] Theoretical predictions suggest that the LSPR λ_{max} cannot be correctly modeled without accounting for the effect of the substrate dielectric constant.[103] The refractive index of the substrate was systematically varied by using fused silica (1.46), borosilicate optical glass (1.52), mica (1.6), and specialty SF-10 glass (1.73). AFM investigation of the Ag nanoparticles on the four substrates showed that the nanoparticle shape is independent of the substrate choice, i.e., the Ag metal wets each substrate to approximately the same extent. The importance of geometric similarity is apparent from previous discussions of LSPR λ_{max} sensitivity to nanoparticle size and shape. The LSPR λ_{max} was measured for each sample in a controlled environment, and results demonstrated a red shift for increasing substrate refractive index (Figure 17). When the LSPR λ_{max} for each substrate was plotted versus the refractive index, a straight line could be fitted to the experimental points, indicating a sensitivity of 87 nm per substrate RIU.

Earlier, it was demonstrated that high aspect ratio nanoparticles are most sensitive to changes in environmental refractive index (Figure 15). It was hypothesized that high aspect ratio nanoparticles would exhibit similarly enhanced sensitivity to the refractive index of the substrate. This was tested by exposing identical SL PPAs deposited on the four aforementioned substrates (fused silica, borosilicate glass, mica, and SF-10 specialty glass) to a variety of refractive index environments.[102] Plots of solvent refractive index verses the LSPR λ_{max} peak shift establish sensitivities of 238, 229, 206, and 258 nm/RIU, respectively (Figure 18). Interestingly, there appears to be no correlation between substrate refractive index and the contribution to solvent sensitivity. Also, the sensitivity gained by using the substrate with the highest sensitivity factor (SF-10) versus the substrate with the lowest sensitivity factor (mica) is only a 25% advantage. One concludes that, although there is slightly improved sensitivity of the LSPR to the external dielectric environment when the Ag nanoparticle is deposited on a high refractive index substrate, the advantage is not sufficient to justify the use of the expensive SF-10 substrate ($15/sample) in place of other inexpensive substrates such as borosilicate glass ($0.25/sample).

3.8. Effect of Molecular Adsorbates on the LSPR. The considerable LSPR sensitivity discovered upon varying the nanoparticle dielectric environment suggested that Ag nanoparticles might be capable of acting as a chemical and/or biological sensor by detecting changes in local refractive index caused by the chemisorption of molecular adsorbates or the binding of biological molecules to an appropriately surface-modified nanoparticle. To test this idea, a series of experiments designed to measure the shift in the LSPR λ_{max} as a function of

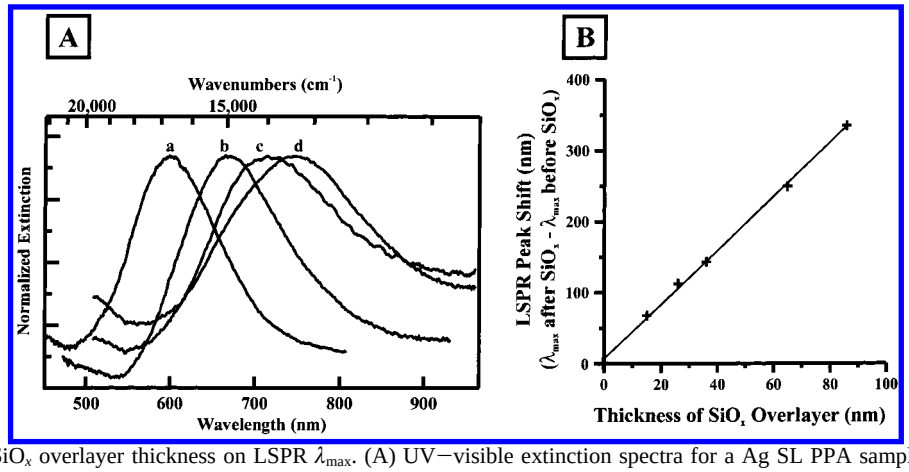

Figure 16. Effect of SiO_x overlayer thickness on LSPR λ_{max}. (A) UV−visible extinction spectra for a Ag SL PPA sample (D = 400 nm and d_m = 25 nm) on glass with various SiO_x overlayer thickness: (a) No SiO_x overlayer; λ_{max} = 597 nm, (b) SiO_x overlayer thickness = 15 nm; λ_{max} = 669 nm, (c) SiO_x overlayer thickness = 26 nm; λ_{max} = 714 nm; (d) SiO_x overlayer thickness = 36 nm; λ_{max} = 745 nm. (B) Plot of LSPR peak shift, $\Delta\lambda_{max}$, versus SiO_x overlayer thickness. The slope of the linear fit of the data indicates that λ_{max} shifts to the red 4 nm for every 1 nm of deposited SiO_x.

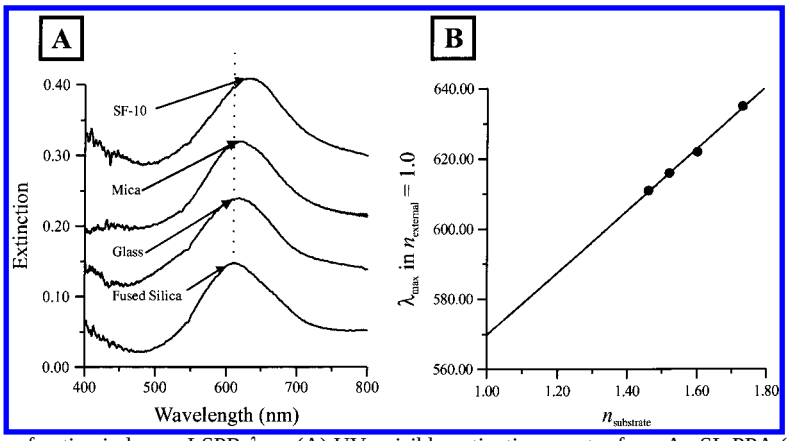

Figure 17. Effect of substrate refractive index on LSPR λ_{max}. (A) UV−visible extinction spectra for a Ag SL PPA (D = 400 nm and d_m = 25 nm) on various substrates. (B) LSPR λ_{max} of Ag SL PPA in a N_2 environment versus the refractive index of the substrate, $n_{substrate}$. Linear regression was used to fit the data to a line described by the following equation: $y = 87x + 483.5$.

alkanethiol SAM chain length was initiated. Alkanethiol SAMs were chosen for this study for three reasons: (1) the sulfur of the thiol functionality binds strongly to both Ag and Au surfaces, (2) SAMs are known to form dense, well ordered films on Ag and Au thin films, and (3) the alkanethiol headgroup can be synthetically tailored to capture specific target molecules. Ag SL PPA samples were incubated for 10−24 h in alkanethiol solutions of varying alkane chain length (1-hexadecanethiol, 1-dodecanthiol, 1-decanethiol, 1-octanethiol, 1-hexanethiol, and 1-butanethiol) and then UV−visible extinction spectra were measured for each sample.[104] A plot of the alkanethiol chain length versus the LSPR λ_{max} shift was linear, with a slope corresponding to a LSPR shift of 3 nm for every carbon atom in the alkanethiol chain (Figure 19). Because the refractive index of all neat alkanethiols used here is approximately constant, the linear dependence is attributed entirely to the increased thickness of the SAM spacer with each additional carbon unit. The ability to detect a single CH_2 unit on the alkanethiol molecule further demonstrates the capability to create an LSPR sensor from SL PPA samples. In fact, the 40 nm LSPR shift seen with 1-hexadecanethiol binding results from only 60 000 molecules per nanoparticle. A reasonable extrapolation suggests that optimized experiments on single nanoparticles would have a detection limit of 1500 molecules or 2.5 zmol.

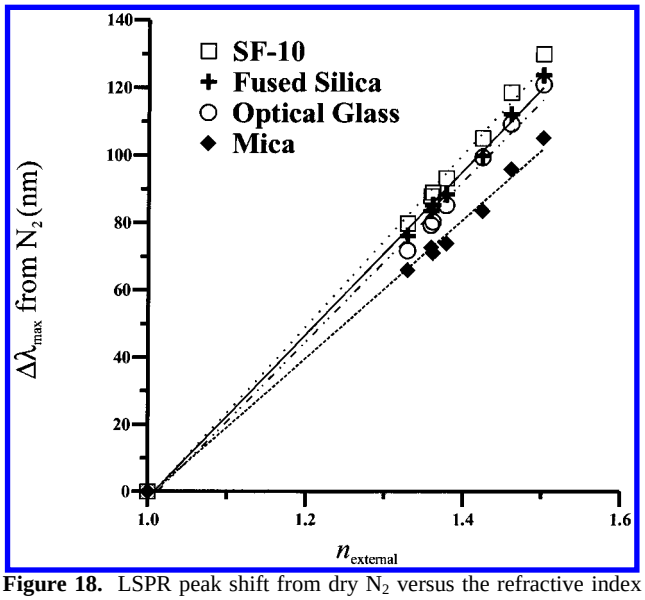

Figure 18. LSPR peak shift from dry N_2 versus the refractive index of the solvent, $n_{external}$, for each of the four substrates. The plotted points represent the average shift recorded for several samples of each substrate. Each data set was fit to a line with the following equations: fused silica, $y = 238x - 241$; borosilicate glass, $y = 229x - 230$; mica, $y = 206x - 208$; SF-10, $y = 258x - 259$.

3.9. Realization of a Ag Nanoparticle LSPR Biosensor. The development of a successful biosensor, based on detecting the shift in the LSPR λ_{max} of a Ag nanoparticle caused by changes in local refractive index, requires that the output signal must be (1) large enough, (2) measurable in an aqueous buffer

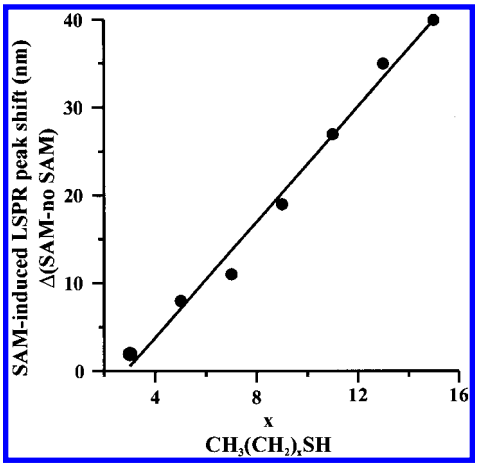

Figure 19. Alkanethiol chain length dependence on LSPR spectral peak shift. All extinction measurements were collected in a N_2 environment. Linear regression was used to fit the data to a line described by the following equation: $y = 3.3x - 9.3$.

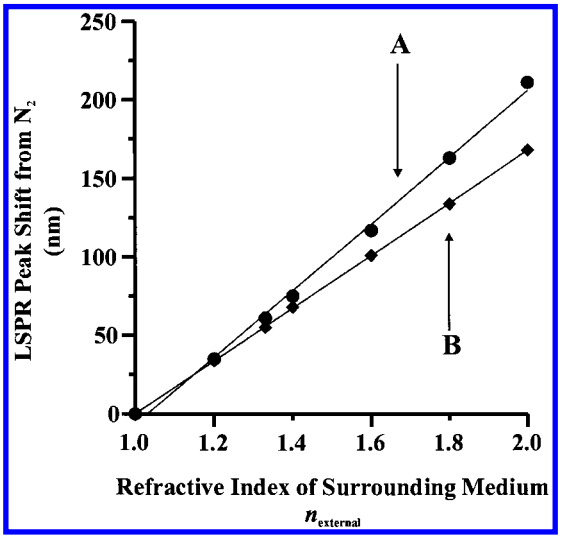

Figure 20. Ag nanoparticle sensitivity to bulk solvent. Spectral peak shifts were calculated by subtracting the measured λ_{max} for the nanoparticles in solvents of $n_{external}$ ranging from 1.33 (methanol) to 1.51 (benzene) from that of a N_2 environment ($n_{external} = 1.0$). Plots display representative measurements from several experiments. (A) Unmodified nanoparticles. The slope of the linear fit shows that the LSPR spectral sensitivity to $n_{external}$ is 191 nm per RIU. (B) Nanoparticles modified with 1-HDT. The slope of the linear fit is reduced by 20% to 150 nm per RIU.

environment, (3) reversible for an actual biological binding event, and (4) insensitive to nonspecific binding. The alkanethiol chain length study discussed in section 3.8 demonstrates that the first condition is fulfilled.

Successful operation of the LSPR nanobiosensor in a solution environment was demonstrated by measuring the sensitivity to changes in local refractive index that occur at the SAM/bulk liquid interface. A decrease in LSPR λ_{max} shift sensitivity was anticipated because the strength of the locally enhanced EM fields are known to decay over a length scale of ~50 nm.[105] To investigate the attenuation of LSPR λ_{max} shift sensitivity by the SAM, the LSPR λ_{max} shift was monitored as changes in the refractive index of the bulk liquid were produced by exposing the unmodified and SAM modified Ag nanoparticles to methanol, acetone, ethanol, methylene chloride, and benzene (Figure 20). These measurements were made in a previously described macroextinction flow cell.[104] For both cases, the sensitivity to the external environment is linearly dependent on

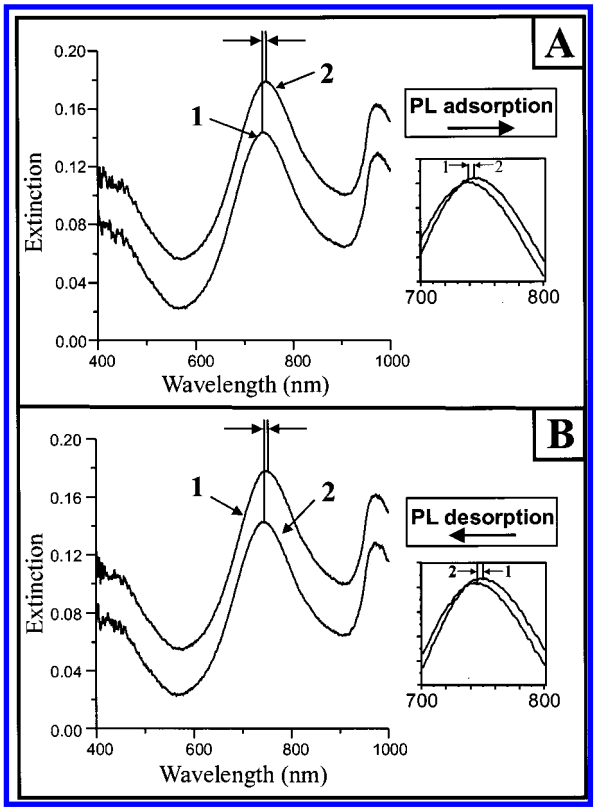

Figure 21. LSPR detected absorption/desorption of PL to 11-MUA/1-OT mixed SAM. (A) PL adsorption. 1. Extinction spectrum of 11-MUA/1-OT modified Ag nanoparticles ($D = 400$ nm and $d_m = 50$ nm) in 5 mM phosphate buffer, pH = 8.5; $\lambda_{max} = 744.6$ nm. 2. Extinction spectrum after incubation with PL (1 mM in lysine); $\lambda_{max} = 749.8$ nm. (B) PL desorption. 1. Extinction spectrum of 11-MUA/1-OT modified Ag nanoparticles with adsorbed PL in 5 mM phosphate buffer, pH = 8.5; $\lambda_{max} = 749.8$ nm. 2. Extinction spectrum after introducing high ionic strength buffer (20 mM phosphate buffered saline; 278 mM NaCl; 5.7 mM KCl); $\lambda_{max} = 744.9$ nm.

the refractive index of the solvent. From the slopes of the linear fits, sensitivity factors of 191 nm/RIU and 150 nm/RIU are extracted from the unmodified and 1-hexadecanethiol modified Ag nanoparticles, respectively. Thus, the presence of the thickest SAM diminishes the LSPR λ_{max} shift sensitivity to the refractive index by approximately 20%. Although the sensitivity is diminished with the SAM spacer, bulk solvent induced shifts are still easily detected, reinforcing the concept that the EM fields extend from the nanoparticle beyond the SAM/bulk liquid interface.

A proof-of-concept experiment was designed and carried out to demonstrate a reversible output signal for an actual biological binding event. The LSPR λ_{max} shift of Ag SL PPA nanoparticles dosed with a mixed monolayer of 11-mercaptoundecanoic acid (11-MUA) and 1-octanethiol (1-OT) was monitored to detect the binding of the multiply charged polypeptide, poly-(L)-lysine (PL). In this well-characterized model system, the positively charged ammonium groups of the lysine residues electrostatically bind to the negatively charged surface provided by the deprotonated carboxylic acid groups of the 11-MUA.[106,107] Upon flowing the PL into the presence of the 1:3 11-MUA/1-OT coated SL PPA, the LSPR λ_{max} shifted 5 nm to the red (Figure 21A). To examine the reversibility of this nanosensor, high ionic strength buffer was flowed into the PL/SAM/SL PPA system. The high ionic strength buffer was expected to screen the ammonium−carboxylate ion pair formation, causing the PL to desorb from the SAM/bulk liquid interface. In fact, the LSPR

λ_{max} shifts the expected 5 nm to the blue, demonstrating that the nanoparticle sensor can be regenerated after each sensing event.

At first, it seemed that the 5 nm shift due to PL binding was rather small. Upon subsequent analysis, it was found to be the correct order of magnitude. The LSPR shift caused by changes in the refractive index of the local environment during the binding and release of PL can be estimated using the following equation:[104]

$$\Delta\lambda_{max} = m(n_{PL} - n_{H_2O})[1 - \exp(-t_{PL}/l_d)] \qquad (6)$$

where m is slope from Figure 20B, $\Delta\lambda_{max}/\Delta n_{external} = 150$ nm/RIU, n_{PL} is the refractive index of PL (1.52), n_{H_2O} is the refractive index of H_2O (1.33), t_{PL} is the thickness of the PL shell on the Ag nanoparticle, and l_d is the characteristic decay length of the LSPR (~20 nm). Assuming that $t_{PL} < l_d$, this equation yields a predicted $\Delta\lambda_{max}$ of 1.4 nm, a factor of 3 to 4 smaller than the measured $\Delta\lambda_{max}$. This discrepancy is most likely due to uncertainties in the estimation of t_{PL} and l_d values. Further experimental and theoretical work will refine the quantitative understanding of the LSPR shift. This simple estimation, however, yields an important conclusion: the LSPR shift is attributable to refractive index changes on the length scale of l_d, a very short length scale of 20 nm or less according to Mie theory estimations.

Although reversibility is an important characteristic, practical biosensors must respond only to the selected target molecule. To verify that the LSPR λ_{max} shift was not due to nonspecific binding, the LSPR λ_{max} shift was monitored after incubation in PL with unmodified SL PPAS and SAM modified SL PPAs. No shift occurred in the unmodified system supporting the SL PPA/SAM system as a potentially successful sensor. Substantial additional testing, now underway, is required to fully validate this new class of nanobiosensors.

4. Conclusions and Closing Remarks

Section 2 of this paper has clearly demonstrated the multitude of nanoparticle structural motifs accessible using NSL. Possible applications of these nanostructures as data storage media, components for future nanoelectronic systems, and substrates for surface-enhanced Raman spectroscopy have been suggested. Undoubtedly, many other applications can be imagined that exploit the simplicity, cost-effectiveness (<$1 per sample), and versatility of this novel nanofabrication method.

Section 3 of this paper recounts the systematic study of the nanoparticle optical properties of silver that is enabled by NSL. This work has demonstrated, for the first time, how the LSPR depends on nanoparticle material, size, shape, interparticle spacing, substrate, solvent, dielectric thin film overlayers, and molecular adsorbates. The following conclusions can be drawn from this systematic study of the LSPR of Ag nanoparticles: (1) the wavelength corresponding to the extinction maximum, λ_{max}, of the LSPR can be systematically tuned from ~400 to 6000 nm with sensitivities of 2−6 optical nanometers per 1 nm variation in nanoparticle width or height, (2) the sensitivity of the LSPR λ_{max} to the refractive index of the supporting substrate is 87 optical nanometers per substrate RIU, (3) the sensitivity of the LSPR λ_{max} to the refractive index of a solvent overlayer is as high as 200 optical nanometers per solvent RIU, (4) the sensitivity of the LSPR λ_{max} to the refractive index of a solvent overlayer is not significantly affected by variance in substrate choice, (5) the LSPR λ_{max} shifts 4 optical nanometers to the red for each nanometer of deposited SiO_x overlayer, (6) the LSPR λ_{max} shifts 3 optical nanometers to the red for each carbon in an adsorbed alkanethiol molecule, and (7) the Ag SL PPA acts as a reversible nanobiosensor. The size, shape, and dielectric-dependent nanoparticle optical properties reported here are likely to have significant impact in conventional and single molecule SERS, near-field optical microscopy, nanoscopic object manipulation, chemical and biological sensing, and energy transport in nanoscopic optical devices.

Acknowledgment. Funding for this work was provided by the ARO (Grant DAAG55-97-1-0133), NSF (Grant CHE-940078), and the MRSEC program of the NSF (Grants DMR-9632472 and DMR-0076097). The authors wish to acknowledge the experimental work contributed to this compilation by David A. Treichel, Matthew T. Smith, Traci R. Jensen, and Michelle Duval Malinsky. The authors also wish to thank Professor George C. Schatz for his many contributions to this work.

References and Notes

(1) Peercy, P. S. *Nature* **2000**, *406*, 1023−1026.
(2) *Clusters and Colloids From Theory to Applications*; Schmid, G., Ed.; VCH Publishers: New York, 1994; p 555.
(3) Steigerwald, M. L.; Brus, L. E. *Acc. Chem. Res.* **1990**, *23*, 183−188.
(4) Brus, L. E.; Trautman, J. K. *Philos. Trans. R. Soc. London, Ser. A* **1995**, *353*, 313−321.
(5) Alivisatos, A. P. *J. Phys. Chem.* **1996**, *100*, 13226−13239.
(6) Alivisatos, A. P. *Science* **1996**, *271*, 933−937.
(7) Reed, M. A.; Kirk, W. P. *Nanostructures and Mesoscopic Systems*; Academic Press, Inc.: San Diego, CA, 1991.
(8) Sundaram, M.; Chalmers, S. A.; Hopkins, P. F.; Gossard, A. C. *Science* **1991**, *254*, 1326−1335.
(9) Benedek, G.; Martin, T. P.; Pacchioni, G. *Elemental and Molecular Clusters*, Springer Series in Materials Science ed.; Springer-Verlag: Berlin, 1988; Vol. 6.
(10) Moskovits, M. *Annu. Rev. Phys. Chem.* **1991**, *42*, 465−499.
(11) de Heer, W. A. *Rev. Mod. Phys.* **1993**, *65*, 611−676.
(12) Castleman, A. W.; Bowen, K. H. *J. Phys. Chem.* **1996**, *100*, 12911−12944.
(13) Mulvaney, P. *Langmuir* **1996**, *12*, 788−800.
(14) Grabar, K. C.; Smith, P. C.; Musick, M. D.; Davis, J. A.; Walter, D. G.; Jackson, M. A.; Guthrie, A. P.; Natan, M. J. *J. Am. Chem. Soc.* **1996**, *118*, 1148−1153.
(15) Feldstein, M. J.; Keating, C. D.; Liau, Y.-H.; Natan, M. J.; Scherer, N. F. *J. Am. Chem. Soc.* **1997**, *119*, 6638−6647.
(16) Kreibig, U. Optics of Nanosized Metals. In *Handbook of Optical Properties. Optics of Small Particles, Interfaces, and Surfaces*; Hummel, R. E., Wissmann, P., Eds.; CRC Press: Boca Raton, FL, 1997; Vol. II, pp 145−190.
(17) New, R. M. H.; Pease, R. F. W.; White, R. L. *J. Vac. Sci. Technol. B* **1995**, *13*, 1089−1094.
(18) Shi, J.; Gider, S.; Babcock, K.; Awschalom, D. D. *Science* **1996**, *271*, 937−941.
(19) Bradley, J. S. The Chemistry of Transition Metal Colloids. In *Clusters and Colloids From Theory to Applications*; Schmid, G., Ed.; VCH Publishers: New York, 1994; pp 459−544.
(20) Street, S. C.; Xu, C.; Goodman, D. W. *Annu. Rev. Phys. Chem.* **1997**, *48*, 43−68.
(21) Heiz, U.; Vanolli, F.; Sanchez, A.; Schneider, W.-D. *J. Am. Chem. Soc.* **1998**, *120*, 9668−9671.
(22) Yang, M. X.; Gracias, D. H.; Jacobs, P. W.; Somorjai, G. A. *Langmuir* **1998**, *14*, 1458−1464.
(23) Volokitin, Y.; Sinzig, J.; de Jongh, L. J.; Schmid, G.; Vargaftik, M. N.; Moiseev, I. I. *Nature* **1996**, *384*, 621−623.
(24) Wang, Z. L.; Petroski, J. M.; Green, T. C.; El-Sayed, M. A. *J. Phys. Chem. B* **1998**, *102*, 6145−6151.
(25) Gorer, S.; Ganske, J. A.; Hemminger, J. C.; Penner, R. M. *J. Am. Chem. Soc.* **1998**, *130*, 9584−9593.
(26) Bezryadin, A.; Dekker, C.; Schmid, G. *Appl. Phys. Lett.* **1997**, *71*, 1273−1275.
(27) Andres, R. P.; Bielefeld, J. D.; Henderson, J. I.; Janes, D. B.; Kolagunta, V. R.; Kubiak, C. P.; Mahoney, W. J.; Osifchin, R. G. *Science* **1996**, *273*, 1690−1693.
(28) Flaugh, P. L.; O'Donnell, S. E.; Asher, S. A. *Appl. Spectrosc.* **1984**, *38*, 847−850.
(29) Munro, C. H.; Pajcini, V.; Asher, S. A. *Appl. Spectrosc.* **1997**, *51*, 1722−1729.

(30) Zou, S.; Williams, C. T.; Chen, E. K.-Y.; Weaver, M. J. *J. Am. Chem. Soc.* **1998**, *120*, 3811−3812.
(31) Emory, S. R.; Haskins, W. E.; Nie, S. *J. Am. Chem. Soc.* **1998**, *120*, 8009−8010.
(32) Emory, S. R.; Nie, S. *J. Phys. Chem. B* **1998**, *102*, 493−497.
(33) Kahl, M.; Voges, E.; Kostrewa, S.; Viets, C.; Hill, W. *Sens. Actuators, B* **1998**, *51*, 285−291.
(34) Zhu, J.; Xu, F.; Schofer, S. J.; Mirkin, C. A. *J. Am. Chem. Soc.* **1997**, *119*, 235−236.
(35) Pipino, A. C. R.; Schatz, G. C.; Van Duyne, R. P. *Phys. Rev. B* **1996**, *53*, 4162−4169.
(36) Yang, W. H.; Hulteen, J. C.; Schatz, G. C.; Van Duyne, R. P. *J. Chem. Phys.* **1996**, *104*, 4313−4323.
(37) Freeman, R. G.; Grabar, K. C.; Allison, K. J.; Bright, R. M.; Davis, J. A.; Guthrie, A. P.; Hommer, M. B.; Jackson, M. A.; Smith, P. C.; Walter, D. G.; Natan, M. J. *Science* **1995**, *267*, 1629−1632.
(38) Caldwell, W. B.; Chen, K.; Herr, B. R.; Mirkin, C. A.; Hulteen, J. C.; Van Duyne, R. P. *Langmuir* **1994**, *10*, 4109−4115.
(39) Van Duyne, R. P.; Hulteen, J. C.; Treichel, D. A. *J. Chem. Phys.* **1993**, *99*, 2101−2115.
(40) Liao, P. F.; Bergman, J. G.; Chemla, D. S.; Wokaun, A.; Melngailis, J.; Hawryluk, A. M.; Economou, N. P. *Chem. Phys. Lett.* **1981**, *81*, 355−359.
(41) Liao, P. F. Silver Structures Produced by Microlithography. In *Surface Enhanced Raman Scattering*; Chang, R. K., Furtak, T. E., Eds.; Plenum Press: New York, 1982; pp 379−390.
(42) Howard, R. E.; Liao, P. F.; Skocpol, W. J.; Jackel, L. D.; Craighead, H. G. *Science* **1983**, *221*, 117−121.
(43) Storhoff, J. J.; Elghanian, R.; Mucic, R. C.; Mirkin, C. A.; Letsinger, R. L. *J. Am. Chem. Soc.* **1998**, *120*, 1959−1964.
(44) Elghanian, R.; Storhoff, J. J.; Mucic, R. C.; Letsinger, R. L.; Mirkin, C. A. *Science* **1997**, *277*, 1078−1081.
(45) Mucic, R. C.; Storhoff, J. J.; Letsinger, R. L.; Mirkin, C. A. *Nature* **1996**, *382*, 607−609.
(46) Bruchez, M., Jr.; Moronne, M.; Gin, P.; Weiss, S.; Alivisatos, A. P. *Science* **1998**, *281*, 2013−2018.
(47) Chan, W. C. W.; Nie, S. *Science* **1998**, *281*, 2016−2018.
(48) Pan, G.; Kesavamoorthy, R.; Asher, S. A. *J. Am. Chem. Soc.* **1998**, *120*, 6525−6530.
(49) Weissman, J. M.; Sunkara, H. B.; Tse, A. S.; Asher, S. A. *Science* **1996**, *274*, 959−960.
(50) Asher, S.; Chang, S.-Y.; Tse, A.; Liu, L.; Pan, G.; Wu, Z.; Li, P. *Mater. Res. Soc. Symp. Proc.* **1995**, *374*, 305−310.
(51) Mansour, K.; Soileau, M. J.; Van Stryland, E. W. *J. Opt. Soc. Am. B* **1992**, *9*, 1100−1109.
(52) Woileau, M. J. *Proceedings of SPIE−The International Society for Optical Engineering. Materials for Optical Switches, Isolators, and Limiters*; SPIE: Washington, DC, 1989; Vol. 1105.
(53) Lidorikis, E.; Li, Q.; Soukoulis, C. M. *Phys. Rev. E* **1997**, *55*, 3613−3618.
(54) Neuendorf, R.; Quinten, M.; Kreibig, U. *J. Chem. Phys.* **1996**, *104*, 6348−6354.
(55) Schubert, E. F.; Hunt, N. E. J.; Micovic, M.; Malik, R. J.; Sivco, D. L.; Cho, A. Y.; Zydzik, G. J. *Science* **1994**, *265*, 943−945.
(56) Wanke, M. C.; Lehmann, O.; Müller, K.; Wen, Q.; Stuke, M. *Science* **1997**, *275*, 1284−1286.
(57) Joannopoulos, J. D.; Villeneuve, P. R.; Fan, S. *Nature* **1997**, *386*, 143−149.
(58) Wallraff, G. M.; Hinsberg, W. D. *Chem. Rev.* **1999**, *99*, 1801−1821.
(59) Ito, T.; Okazaki, S. *Nature* **2000**, *406*, 1027−1031.
(60) Bloomstein, T. M.; Horn, M. W.; Rothschild, M.; Kunz, R. R.; Palmacci, S. T.; Goodman, R. B. *J. Vac. Sci. Technol. B* **1997**, *15*, 2112−2116.
(61) Kitson, S. C.; Barnes, W. L.; Sambles, J. R. *IEEE Photonics Technol. Lett.* **1996**, *8*, 1662−1664.
(62) Smith, H. I.; Schattenburg, M. L. *IBM J. Res. Dev.* **1993**, *37*, 319−329.
(63) Stroscio, J. A.; Eigler, D. M. *Science* **1991**, *254*, 1319−1326.
(64) Liu, G.-Y.; Xu, S.; Qian, Y. *Acc. Chem. Res.* **2000**, *33*, 457−466.
(65) Piner, R. D.; Zhu, J.; Xu, F.; Hong, S.; Mirkin, C. A. *Science* **1999**, *283*, 661−663.
(66) Roder, H.; Hahn, E.; Brune, H.; Bucher, J.-P.; Kern, K. *Nature* **1993**, *366*, 141−143.
(67) Li, A.; Liu, F.; Petrovykh, D. Y.; Lin, J.-L.; Viernow, J.; Himpsel, F. J.; Lagally, M. G. *Phys. Rev. Lett.* **2000**, *85*, 5380−5383.
(68) Zach, M. P.; Ng, K. H.; Penner, R. M. *Science* **2000**, *290*, 2120−2123.
(69) McClelland, J. J.; Scholten, R. E.; Palm, E. C.; Celotta, R. J. *Science* **1993**, *262*, 877−880.
(70) Deckman, H. W.; Dunsmuir, J. H. *Appl. Phys. Lett.* **1982**, *41*, 377−379.
(71) Fischer, U. C.; Zingsheim, H. P. *J. Vac. Sci. Technol.* **1981**, *19*, 881−885.
(72) Deckman, H. W.; Dunsmuir, J. H. *J. Vac. Sci. Technol. B* **1983**, *1*, 1109−1112.
(73) Roxlo, C. B.; Deckman, H. W.; Ables, B. *Phys. Rev. Lett.* **1986**, *57*, 2462−2465.
(74) Deckman, H. W.; Dunsmuir, J. H. Natural Lithographic Fabrication of Microstructures over Large Areas. In *Patent*; Exxon Research and Engineering Co.: Florham Park, NJ, 1987.
(75) Deckman, H. W.; Moustakas, T. D. *J. Vac. Sci. Technol. B* **1988**, *6*, 316−318.
(76) Deckman, H. W.; Dunsmuir, J. H.; Garoff, S.; McHenry, J. A.; Peiffer, D. G. *J. Vac. Sci. Technol. B* **1988**, *6*, 333−336.
(77) Hulteen, J. C.; Van Duyne, R. P. *J. Vac. Sci. Technol. A* **1995**, *13*, 1553−1558.
(78) Hulteen, J. C.; Treichel, D. A.; Smith, M. T.; Duval, M. L.; Jensen, T. R.; Van Duyne, R. P. *J. Phys. Chem. B* **1999**, *103*, 3854−3863.
(79) Micheletto, R.; Fukuda, H.; Ohtsu, M. *Langmuir* **1995**, *11*, 3333−3336.
(80) Rugar, D.; Mamin, H. J.; Lambert, S. E.; Stern, J. E.; McFadyen, I.; Yogi, T. *J. Appl. Phys.* **1990**, *68*, 1169−1183.
(81) Krause, F.; Kaisinger, F.; Starke, H.; Persch, G.; Hartmann, U. *Thin Solid Films* **1995**, *264*, 141−147.
(82) Haynes, C. L.; Haes, A. J.; Van Duyne, R. P. *Mater. Res. Soc. Symp. Proc.* **2001**, in press.
(83) Kneipp, K.; Wang, Y.; Kneipp, H.; Perelman, L. T.; Itzkan, I.; Dasari, R. R.; Feld, M. S. *Phys. Rev. Lett.* **1997**, *78*, 1667−1670.
(84) Nie, S.; Emory, S. R. *Science* **1997**, *275*, 1102−1106.
(85) Michaels, A. M.; Nirmal, M.; Brus, L. E. *J. Am. Chem. Soc.* **1999**, *121*, 9932−9939.
(86) Dickmann, J.; Geyer, A.; Daembkes, H.; Nickel, H.; L"sch, R.; Schlapp, W. *J. Electrochem. Soc.* **1991**, *138*, 491−493.
(87) Strifler, W. A.; Cantos, B. D. *J. Vac. Sci. Technol. B* **1990**, *8*, 1297−1299.
(88) Kenyon, M.; Amar, A.; Song, D.; Lobb, C. J.; Wellstood, F. C. *Appl. Phys. Lett.* **1998**, *72*, 2268−2270.
(89) Wada, T.; Haraichi, S.; Ishii, K.; Hiroshima, H.; Komuro, M.; Hirayama, M. *J. Vac. Sci. Technol. A* **1996**, *14*, 1850−1854.
(90) Wada, T.; Haraichi, S.; Ishii, K.; Hiroshima, H.; Komuro, M.; Gorwadkar, S. M. *J. Vac. Sci. Technol. A* **1998**, *16*, 1430−1434.
(91) Mbise, G. W.; Le Bellac, D.; Niklasson, G. A.; Granqvist, C. G. *J. Phys. D: Appl. Phys.* **1997**, *30*, 2103-2122.
(92) Moskovits, M. *Rev. Mod. Phys.* **1985**, *57*, 783−826.
(93) Otto, A.; Mrozek, I.; Grabhorn, H.; Akemann, W. *J. Phys. Condens. Matter* **1992**, *4*, 1143−1212.
(94) Campion, A.; Kambhampati, P. *Chem. Soc. Rev.* **1998**, *27*, 241−250.
(95) Schatz, G. C.; Van Duyne, R. P. Electromagnetic Mechanism of Surface-Enhanced Spectroscopy. In *Handbook of Vibrational Spectroscopy*; Griffiths, P. R., Ed.; Wiley: New York, 2001; in press.
(96) Kreibig, U.; Vollmer, M. *Optical Properties of Metal Clusters*; Springer-Verlag: Heidelberg, Germany, 1995; Vol. 25.
(97) Link, S.; El-Sayed, M. A. *J. Phys. Chem. B* **1999**, *103*, 8410−8426.
(98) Jensen, T. R.; Van Duyne, R. P.; Johnson, S. A.; Maroni, V. A. *Appl. Spectrosc.* **2000**, *54*, 371−377.
(99) Jensen, T. R.; Duval Malinsky, M.; Haynes, C. L.; Van Duyne, R. P. *J. Phys. Chem. B* **2000**, *104*, 10549−10556.
(100) Jensen, T. R.; Schatz, G. C.; Van Duyne, R. P. *J. Phys. Chem. B* **1999**, *103*, 2394−2401.
(101) Jensen, T. R.; Duval, M. L.; Kelly, L.; Lazarides, A.; Schatz, G. C.; Van Duyne, R. P. *J. Phys. Chem. B* **1999**, *103*, 9846−9853.
(102) Duval Malinsky, M.; Kelly, L.; Schatz, G. C.; Van Duyne, R. P. *J. Phys. Chem. B* **2001**, *105*, 2343−2350.
(103) Kelly, L.; Jensen, T. R.; Lazarides, A.; Schatz, G. C. Modeling Nanoparticle Optical Properties. In *Metal Nanoparticles: Synthesis, Characterization and Applications*; Feldheim, D. L., Foss, C. A., Jr., Eds.; Marcel-Dekker: New York, 2001; in press.
(104) Duval Malinsky, M.; Kelly, L.; Schatz, G. C.; Van Duyne, R. P. *J. Am. Chem. Soc.* **2001**, *123* (7), 1471−1482.
(105) Jensen, T. R.; Kelly, L.; Lazarides, A.; Schatz, G. C. *J. Clust. Sci.* **1999**, *10*, 295−317.
(106) Frey, B. L.; Jordan, C. E.; Kornguth, S.; Corn, R. M. *Anal. Chem.* **1995**, *67*, 4452−4457.
(107) Frey, B. L.; Corn, R. M. *Anal. Chem.* **1996**, *68*, 3187−3193.